Microtubule dynamics regulates mitochondrial fission

Kritika Mehta[1], Manjyot Kaur Chug[1], Siddharth Jhunjhunwala[1] and Vaishnavi Ananthanarayanan[1,*]

[1] *Centre for BioSystems Science and Engineering, Indian Institute of Science, Bangalore 560012*

** To whom correspondence may be addressed. Email: vaishnavi@iisc.ac.in*

Abstract

Mitochondria are organised as tubular networks in the cell and undergo fission and fusion. Equilibrium between fission and fusion events is necessary to maintain normal mitochondrial function. While several of the molecular players involved in mediating the dynamics of mitochondria have been identified, the precise cellular cues that initiate fission or fusion remain largely unknown. In fission yeast, as in mammalian cells, mitochondrial positioning and partitioning are microtubule-mediated. In interphase, fission yeast mitochondria associate with microtubule bundles that are aligned along the long axis of the cell. Here, we perturbed microtubule dynamics via kinesin-like proteins to produce cells with long and short microtubules and observed that cells with long microtubules exhibited long, but fewer mitochondria, whereas cells with short microtubules exhibited short, but several mitochondria. We quantified that mitochondrial fission frequency correlated inversely with microtubule length. In agreement with these results, upon onset of mitosis wherein interphase microtubules assemble to form the spindle within the nucleus, we measured increased fission of mitochondria in the absence of interphase microtubules. We confirmed that partitioning of mitochondria at mitosis follows a stochastic, independent segregation mechanism and that the increase in mitochondrial fission prior to cell division therefore likely serves to increase the likelihood of equal partitioning of mitochondria between the two future daughter cells. Further, association of mitochondria with microtubules inhibited activity of the dynamin GTPase-related fission protein Dnm1, such that cells overexpressing Dnm1 but containing long microtubules were protected from increased fission. Thus, we demonstrate a general mechanism by which mitochondrial dynamics is dictated by the dynamics of the microtubule cytoskeleton.

Introduction

Mitochondria are double-membraned organelles whose functions range from ATP production to calcium signalling. Inside cells, mitochondrial form is dynamic and transitions from tubular networks to fragmented entities depending on the activity of the mitochondrial fission and fusion machinery. The major mitochondrial fission protein is dynamin-related Drp1 GTPase[1] (Dnm1 in yeast[2,3]). Multimeric Drp1 rings assemble around the mitochondrial membrane and utilize the energy from GTP hydrolysis to catalyse the constriction and fission of mitochondria[4,5]. Fusion of mitochondria requires two sets of proteins namely Opa1[6] for the inner membrane (Mgm1 in yeast[7]) and Mfn1/2[8] for the outer membrane (Fzo1 in yeast[9]).

The requirement for dynamic mitochondria has been attributed to two primary reasons, namely quality control and energy production[10]. Larger/longer mitochondria resulting from fusion are hypothesized to be capable of producing more energy whereas shorter/smaller mitochondria formed following a fission event are likely to undergo mitophagy[11]. In the case of the latter, fission could serve as an efficient mechanism to segregate and eliminate damaged mitochondria. Dysfunction of fission and fusion processes has been implicated in neurodegeneration[12,13], cancer[14] and cardiomyopathies[15], amongst a host of metabolic disorders.

In mammalian cells, mitochondria are transported along microtubule tracks by the activity of motor proteins kinesin-1 and dynein[16]. Kinesin-1 and dynein bind to the outer membrane of mitochondria via the Miro/Milton complex[17–19] and move mitochondria in the anterograde and retrograde direction respectively. In neuronal cells, increase in calcium levels results in the attachment of kinesin-1 motor to mitochondria via syntaphilin, which inhibits the ATPase activity of kinesin and hence leads to stationary mitochondria on neuronal microtubules[20]. About 70% of mitochondria in neuronal cells have been visualized in this stationary state[21].

In contrast to mammalian cells, mitochondria in fission yeast do not undergo motor-driven movement along microtubules. However, the protein Mmb1 has been identified to associate mitochondria with dynamic microtubules[22]. Upon microtubule depolymerisation using methyl benzimidazol-2-yl-carbamate (MBC) or deletion of Mmb1, mitochondria have been observed to undergo fragmentation[3,22,23]. Conversely, in cells overexpressing Mmb1, mitochondria seemingly undergo reduced fission and exhibit long mitochondria[22].

Cells employ several strategies to reduce partitioning error of organelles during mitosis, such as ordered segregation mediated by spindle poles, or increasing copy numbers of organelles prior to cell division[24]. In the latter, homogeneous distribution of the multiple organelle copies serves to increase the probability of equal partitioning stochastically. Mitochondrial inheritance has been observed to be microtubule-dependent in mammalian cells[25]. In fission yeast, mitochondrial partitioning during cell division has been proposed to be mediated by attachment of mitochondria with spindle poles[26,27], similar to the segregation of endosomes, lysosomes and Golgi bodies in mammalian cells[28,29] . However, only a portion of the observed mitochondria associated with the spindle poles[26]. Additionally, increased mitochondrial fragmentation upon the onset of mitosis has also been observed[3], perhaps indicating a stochastic mechanism for mitochondrial partitioning.

While the molecular players that effect fission and fusion have been identified in several systems, the cellular signals that regulate these events are largely elusive. Here, we demonstrate that mitochondria piggyback on dynamic microtubules to selectively undergo fission while microtubules depolymerise. Reorganisation of interphase microtubules into the nucleus when cells prepare for division also provided the cue for increased mitochondrial fission. We quantified the number of mitochondria in mother cells immediately after formation of mitotic spindle within the nucleus and the number of mitochondria in the resulting daughter cells, and confirmed that the partitioning was indeed a good fit to a binomial distribution, indicating that the mitochondria were stochastically segregated into the two daughter cells. We observed that the fission protein Dnm1 was excluded from regions of microtubules localisation and that the presence of long and stabilised microtubules was inhibitory to uncontrolled fission even when Dnm1 was overexpressed.

Results

1. Perturbation of microtubule dynamics leads to changes in mitochondrial numbers

We observed that mitochondria underwent increased fission in the absence of microtubules, but did not observe their subsequent aggregation as reported previously (Extended Data Fig. 1a-c). Instead, the fragmented mitochondria were mobile and frequently in close contact with each other (Extended Data Fig. 1b, c, Supplementary Video S1). Since the depolymerisation of microtubules had a direct effect on mitochondrial fission, we set out to study the consequence of modification of microtubule dynamics on mitochondrial dynamics. To this end, we visualised the mitochondria and microtubules of fission yeast strains carrying deletions of antagonistic kinesin-like proteins, Klp5/Klp6 and Klp4 in high-resolution deconvolved images (Fig. 1a, Supplementary Videos S2, S3 and S4).

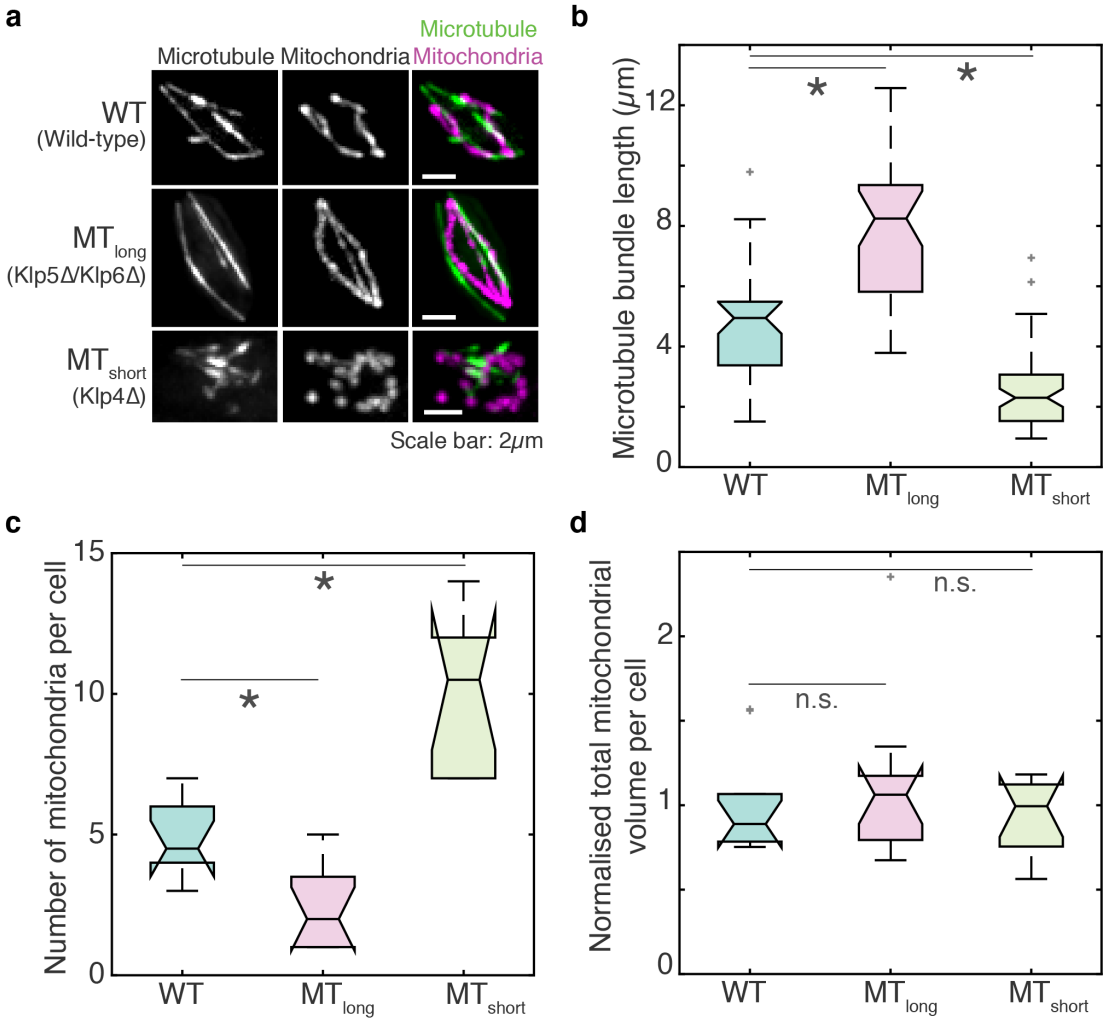

Figure 1. Mitochondrial number is inversely proportional to microtubule length. a, Maximum intensity projections of deconvolved Z-stack images of microtubules (left), mitochondria (centre) and their composite (right) in wild-type ('WT', top, strain KI001, see

Table S1), Klp5Δ/Klp6Δ ('MT_{long}', strain G3B, see Table S1) and Klp4Δ ('MT_{short}', strain G5B, see Table S1) cells. **b,** Box plot of length of anti-parallel microtubule bundles in WT, MT_{long} and MT_{short} cells (*n*=40, 37 and 63 bundles respectively). **c,** Box plot of number of mitochondria per cell in WT, MT_{long} and MT_{short} cells (*n*=10, 12 and 13 cells respectively). **d,** Box plot of the total volume of mitochondria per cell in WT, MT_{long} and MT_{short} cells normalised to mean total wild-type mitochondrial volume (*n*=10, 12 and 13 cells respectively). Light grey crosses represent outliers, asterisk represents significance ($p<0.05$) and 'n.s.' indicates no significant difference.

The heteromeric Klp5/Klp6 motor is required for maintenance of interphase microtubule length by promoting catastrophe at microtubule plus ends[30,31]. Cells lacking Klp5 and Klp6 exhibited long microtubule bundles ('MT_{long}', Fig. 1b) as reported previously due to a decreased catastrophe rate[30]. In contrast, Klp4 is required for polarised growth in fission yeast and has been suggested to promote microtubule growth[32,33]. As a result, in the absence of Klp4, microtubule bundles were only about half the length of wild-type bundles ('MT_{short}', Fig. 1b).

As in wild-type cells, mitochondria in Klp5Δ/Klp6Δ were in close contact with the microtubule, whereas we observed reduced association between the short microtubules and mitochondria in Klp4Δ cells (Fig. 1a, Supplementary Videos S3 and S4). While wild-type cells had 4.9 ± 0.4 (mean ± s.e.m.) mitochondria per cell, we observed that Klp5Δ/Klp6Δ contained only 2.3 ± 0.4 (mean ± s.e.m.). In contrast, Klp4Δ cells had 10 ± 0.9 mitochondria per cell (mean ± s.e.m., Fig. 1c). This indicated that the number of mitochondria per cell was inversely related to the length of microtubule bundle. So too, cells carrying a deletion of the EB1 homologue Mal3 exhibited small microtubule bundles[34] and also contained several mitochondria as reported previously[22] (Extended Data Fig. 1d). However, the decrease in the number of mitochondria in Klp5Δ/Klp6Δ cells and increase in Klp4Δ cells were not at the expense of mitochondrial volume, since the net mitochondrial volume in both cases was comparable to wild-type mitochondrial volume (Fig. 1d, Extended Data Fig. 1e).

2. Cells with short microtubules undergo increased fission

To understand the difference in mitochondrial numbers in wild-type, Klp5Δ/Klp6Δ and Klp4Δ cells, we acquired and analysed time-lapse videos at the single mitochondrion level in all three cases (Fig. 2a, Supplementary Videos S5, S6 and S7). Similar to our observations from high-resolution images, we measured 3.6 ± 0.2, 2.7 ± 0.2, and 6.9 ± 0.8

138 mitochondria (mean ± s.e.m.) in wild-type, Klp5Δ/Klp6Δ and Klp4Δ cells respectively (Fig.
139 1c and 2b). Analysis of evolution of these mitochondrial numbers revealed no significant
140 changes over time (Fig. 2b).

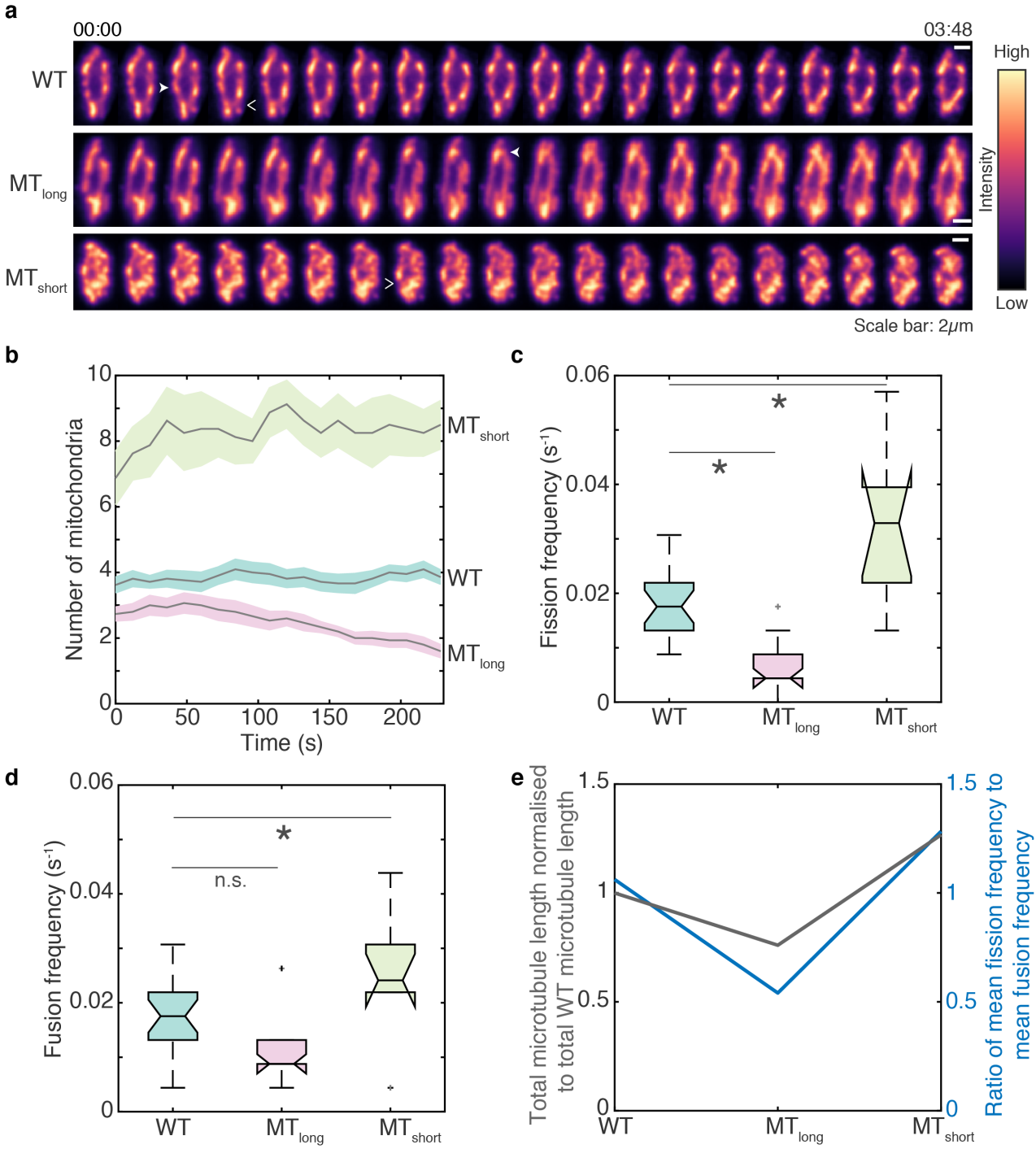

141

142 **Figure 2. Microtubule catastrophe rate determines fission frequency of**
143 **mitochondria. a,** Montage of maximum intensity projected confocal Z-stack images of wild-
144 type ('WT', strain KI001, see Table S1), Klp5Δ/Klp6Δ ('MT_{long}', strain G3B, see Table S1)
145 and Klp4Δ ('MT_{short}', strain G5B, see Table S1) cells represented in the intensity map
146 indicated to the right of the images. White solid arrowheads point to representative fusion
147 events and open arrowheads to fission events. Time is indicated above the images in

mm:ss. **b,** Evolution of mitochondrial number over time indicated as mean (solid grey line) and standard error of the mean (shaded region) for WT, MT_{long} and MT_{short} cells (*n*=21, 15 and 8 cells respectively **c,** Box plot of the fission frequency of mitochondria per second in WT, MT_{long} and MT_{short} cells (*n*=21, 15 and 8 cells respectively). **d,** Box plot of the fusion frequency of mitochondria per second in WT, MT_{long} and MT_{short} cells (*n*=21, 15 and 8 cells respectively). Light grey crosses represent outliers, asterisk represents significance ($p<0.05$) and 'n.s.' indicates no significant difference. **e,** Plot of total microtubule length normalised to total microtubule length in wild-type cells (grey) and ratio of mean fission frequency to mean fusion frequency (blue) in WT, MT_{long} and MT_{short} cells.

Additionally, mitochondria in wild-type cells underwent ~1 fission and ~1 fusion event every minute on an average, whereas Klp5Δ/Klp6Δ cells exhibited a fission frequency that was half that of wild-type, and Klp4Δ mitochondria had a fission frequency that was almost double that of wild-type (Fig. 2c). The fusion frequency of mitochondria in Klp4Δ cells was slightly higher than in wild-type and Klp5Δ/Klp6Δ cells (Fig. 2d), likely due to the increased number of mitochondria in Klp4Δ cells that could participate in fusion. However, the resulting ratio of the mean fission frequency to the mean fusion frequency was ~1, ~0.5 and ~1.3 in wild-type, Klp5Δ/Klp6Δ and Klp4Δ cells respectively. Interestingly, these ratios accurately matched the total microtubule lengths of wild-type, Klp5Δ/Klp6Δ and Klp4Δ cells (19µm, 25µm and 15µm on an average) normalised to total WT microtubule length (1, 0.76 and 1.26 respectively, Fig. 2e). We therefore concluded that the difference in mitochondrial numbers between wild-type cells and Klp5Δ/Klp6Δ and Klp4Δ arose primarily due to the changes in fission frequencies of mitochondria. Note that the rate of mitochondrial fission (per second per mitochondrion) was comparable to the rate of mitochondrial fusion (per second per mitochondrion) in all three cases, which explains the constant number of mitochondria we measured over time (Fig. 2b).

To specifically test the role of microtubules in determining the length and dynamics of mitochondria, we depolymerised microtubules in wild-type and Klp5Δ/Klp6Δ cells and visualised the mitochondria in time-lapse movies (Extended Data Fig. 2a). In both cases, upon microtubule depolymerisation, we observed a switch in mitochondrial morphology to increased numbers and increased fission that was reminiscent of Klp4Δ cells (Extended Data Fig. 2b-h).

Increase in oxidative stress via reactive oxygen species (ROS) levels has also been described to induce mitochondrial fission[35]. However, we measured no difference in ROS levels between wild-type, Klp5Δ/Klp6Δ, and Klp4Δ cells (Extended Data Fig. 2i).

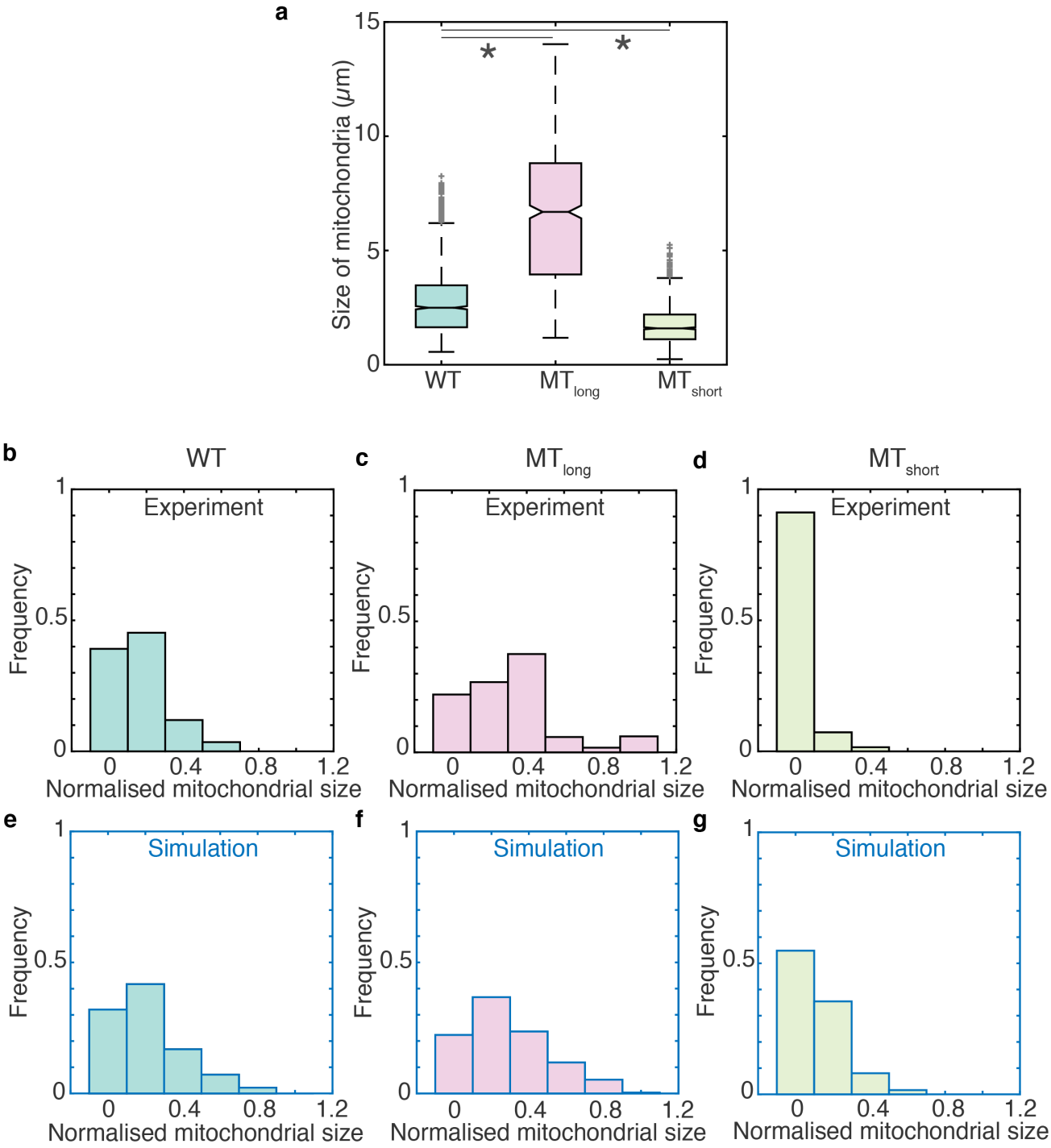

Figure 3. Mitochondrial sizes are predicted by partitioning the same amount of mitochondrial material among different numbers of mitochondria. **a,** Box plot of the size of mitochondria in wild-type ('WT', strain KI001, see Table S1), Klp5Δ/Klp6Δ ('MT_{long}', strain G3B, see Table S1) and Klp4Δ ('MT_{short}', strain G5B, see Table S1) cells, calculated as the length of the major axis of an ellipse fitted to each mitochondrion (n=1613, 739 and 1326 mitochondria respectively). Light grey crosses represent outliers, asterisk represents significance ($p<0.05$) and 'n.s.' indicates no significant difference. **b-d,** Histogram of mitochondrial sizes normalised to total size of mitochondria per cell obtained from experiments in WT, MT_{long} and MT_{short} cells. **e-g,** Histogram of mitochondrial sizes

194 normalised to total size of mitochondria per cell obtained from simulations using numbers of
195 mitochondria measured in WT, MT_{long} and MT_{short} cells.
196
197 **3. Mitochondrial sizes reflect microtubule lengths**
198 Additionally, we observed that the size of an individual mitochondrion correlated with the
199 length of the microtubule bundle in the cell, with Klp5Δ/Klp6Δ cells containing long
200 mitochondria and Klp4Δ cells having short mitochondria. Wild-type cells predictably
201 exhibited mitochondrial size ranges that lay between that of Klp5Δ/Klp6Δ and Klp4Δ cells
202 (Fig. 3a, Extended Data Fig. 3a-c). As detailed in Fig. 1d, the net mitochondrial volume was
203 identical in wild-type, Klp5Δ/Klp6Δ and Klp4Δ cells. We tested the possibility that the
204 mitochondrial size distributions we observed in wild-type, Klp5Δ/Klp6Δ and Klp4Δ cells
205 (Fig. 3b-d) could simply be a consequence of partitioning the same amount of mitochondria
206 into ~4, ~2 and ~7 mitochondria respectively. Fig. 3e-g depicts the results of simulating the
207 possible size distributions that mitochondria could exhibit relative to the total mitochondrial
208 size (see Methods).
209 We observed similar mitochondrial size distributions in both our experiments and
210 simulations reconfirming our earlier observation that the total mitochondrial content remains
211 unchanged between wild-type, Klp5Δ/Klp6Δ and Klp4Δ cells.
212
213 **4. Mitochondria undergo stochastic partitioning during mitosis**
214 Fission yeast undergoes closed mitosis, wherein the nuclear envelope does not undergo
215 breakdown during cell division[36]. Upon onset of mitosis in fission yeast, the interphase
216 microtubules that were previously in the cytoplasm are reorganised to form the spindle
217 inside the closed nucleus. This natural situation mimics the depolymerisation of
218 microtubules via the chemical inhibitor MBC. Therefore, we set out to study the changes in
219 the mitochondrial network upon cell entry into mitosis. We first obtained high-resolution
220 deconvolved images of the microtubule and mitochondria in fission yeast cells undergoing
221 cell division (Fig. 4a, Extended Data Fig. 4a, Supplementary Video S8). We observed that
222 dividing wild-type cells had ~4x the number of mitochondria in interphase cells (Fig. 4b).
223 Moreover, similar to what was seen in cells lacking microtubules or Klp4 (Fig. 1a),
224 mitochondria in dividing cells were shorter and more rounded (Fig. 4a, Extended Data Fig.
225 4a). There was no relationship between length of the mitotic spindle and the number of
226 mitochondria (Fig. 4b, Extended Data Fig. 4a), indicating that the increased fission likely

occurred fairly early upon entry into mitosis. Analysis of time-lapse videos of wild-type cells before and 10min after entry into mitosis revealed a doubling of mitochondrial numbers in this time (Fig. 4c, d, Supplementary Video S9). Note that this is likely an underestimate since we were unable to reliably resolve some of the mitochondria in these lower-resolution images. The fragmented mitochondria appeared more mobile and were able to traverse distances of ~1µm in the cell presumably by Brownian motion (Fig. 4c). In this same period of time, non-dividing interphase cells did not show any change in mitochondrial numbers (Extended Data Fig. 4b, c).

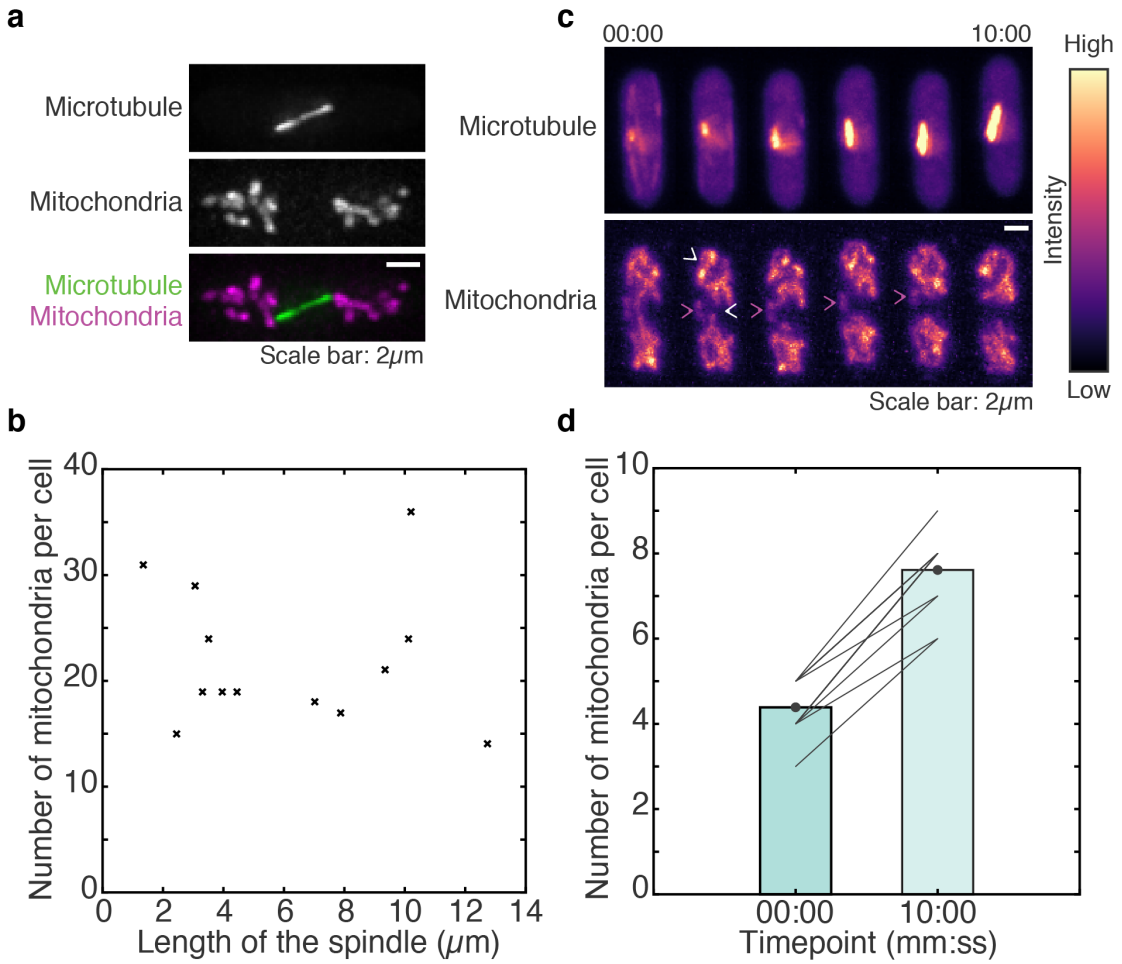

Figure 4. Mitotic cells contain several short mitochondria. a, Maximum intensity projections of deconvolved Z-stack images of the microtubules (top), mitochondria (centre) and their composite (bottom) of a wild-type cell (strain KI001, see Table S1) undergoing division. **b,** Scatter plot of the length of the mitotic spindle vs. the number of mitochondria per cell in dividing cells (*n*=13 cells). **c,** Montage of maximum intensity projected confocal Z-stack images of the microtubules (top) and mitochondria (bottom) in a wild-type cell (strain KI001, see Table S1) undergoing cell division represented in the intensity map indicated to the right of the images. White open arrowheads point to representative fission events. Magenta arrowheads point to a representative mobile, fragmented mitochondrion. Time is indicated above the images in mm:ss. **d,** Bar plot of the mean number of mitochondria per

246 cell before ('00:00') and 10mins after ('10:00') the onset of mitosis. Solid grey lines
247 represent data from individual cells (*n*=16 cells).
248 Increase in mitochondrial numbers prior to cell division could aid in increasing the
249 likelihood of equal partitioning of mitochondria between daughter cells, given a stochastic
250 mechanism. To test if mitochondria in our system underwent stochastic, independent
251 segregation,[24] with each mitochondrion in the mother cell having a 50% chance of
252 segregating to either of the future daughter cells during mitosis, we tested the fit of our data
253 to a binomial distribution[37] using a Chi-square test as previously described[38]. Our data
254 (Table S2) did not differ significantly from a binomial distribution with a Chi-square statistic
255 of 7.1846 with 3 degrees of freedom and p=0.0662, indicating that mitochondria in fission
256 yeast were indeed segregating stochastically during cell division. The increase in
257 mitochondrial numbers upon onset of mitosis also served to reduce the partitioning error of
258 mitochondria between the daughter cells as predicted by stochastic segregation (Extended
259 Data Fig. 4d).
260
261 **5. Dnm1 rings do not localize to the microtubules**
262 Taken together, our results suggest that association of mitochondria with microtubules
263 inhibits mitochondrial fission. The mitochondrial fission protein in yeast is a dynamin-related
264 GTPase, Dnm1[3]. Dnm1 brings about the fission of mitochondria by self-assembling into a
265 ring around the diameter of the mitochondria and employing its GTPase activity to effect the
266 scission[4]. In the absence of Dnm1, mitochondria are organised as extended, fused
267 'nets'[3,39]. We hypothesised that the binding of mitochondria to microtubules physically
268 hinders the formation of a complete ring of Dnm1 around the mitochondrion. To test this
269 hypothesis, we introduced GFP-tagged Dnm1 under the control of the thiamine-repressible
270 nmt1 promoter[40] into wild-type cells expressing fluorescent microtubules (see Table S1). C-
271 or N-terminal tagging of Dnm1 renders it inactive[3] and therefore the scission activity of
272 Dnm1 could not be directly observed (Extended Data Fig. 5a). However, we visualised the
273 localisation of Dnm1 'spots', representing Dnm1 assemblies. We counted a slight decrease
274 in Dnm1 spots in Klp5Δ/Klp6Δ, and ~2x increase in Klp4Δ cells as compared to wild-type
275 cells (Extended Data Fig. 5b), corroborating our previous observations indicating decreased
276 fission in the former and increased fission in the latter (Fig. 2c). Although almost 100% of
277 the Dnm1 spots colocalised with mitochondria (Extended Data Fig. 5a), 85% of the spots

did not localise on the microtubule (Fig. 5a, Supplementary Video S10), indicating that the presence of microtubule had an inhibitory effect on the assembly of the Dnm1 ring.

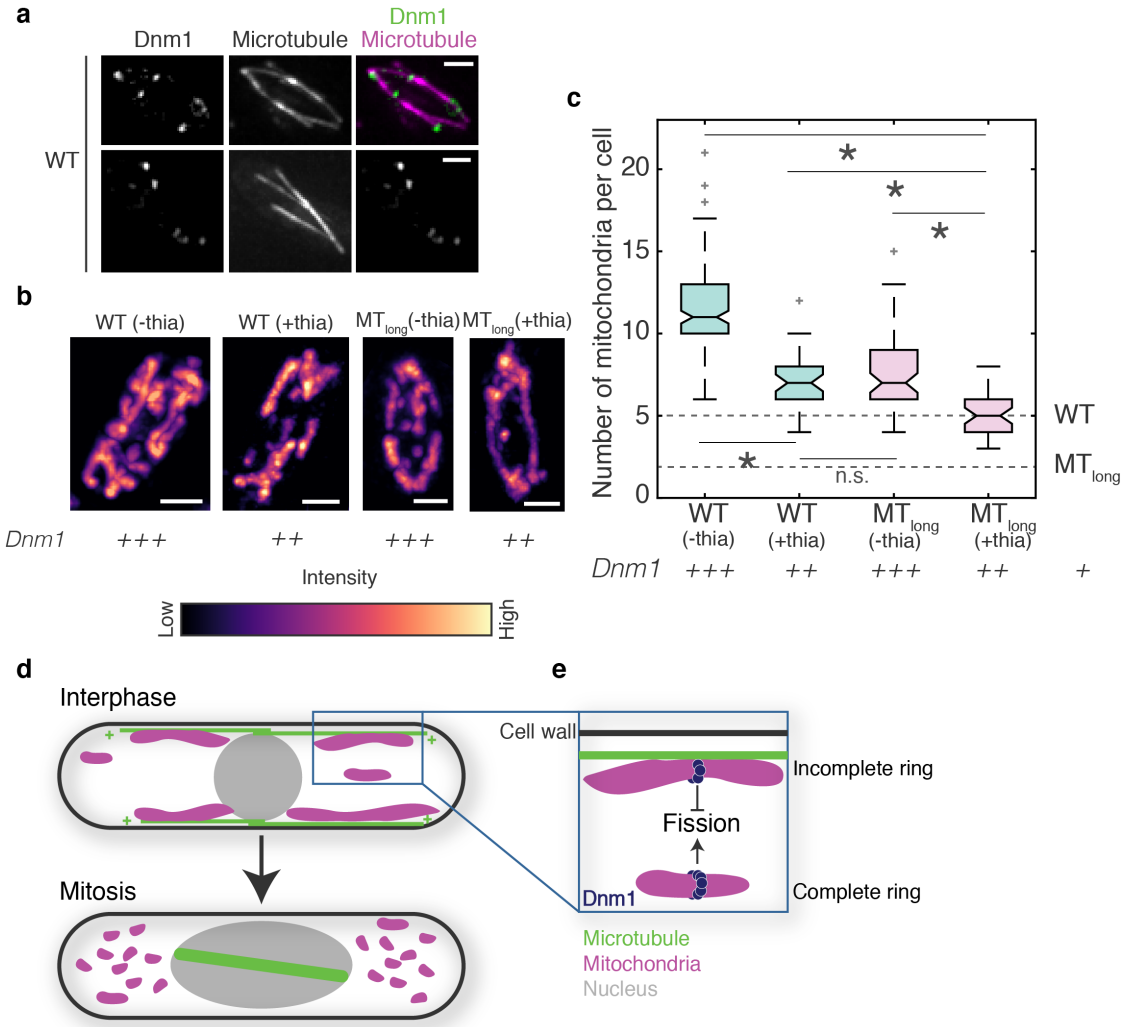

Figure 5. Association with microtubules prevents uncontrolled fission of mitochondria. a, Maximum intensity projections of deconvolved Z-stack images of Dnm1 (left), microtubules (centre) and their composite (right) in wild-type cells expressing fluorescent Dnm1 and tubulin (strain MTY271 transformed with pREP41-Dnm1-Cterm-GFP, see Table S1). A majority of Dnm1 spots did not localise on the microtubule (*n*=14 cells). **b,** Maximum intensity projections of deconvolved Z-stack images of mitochondria in cells transformed with functional untagged Dnm1 (plasmid pREP41-Dnm1, see Table S1) in wild-type ('WT', strain FY7143, see Table S1) and Klp5Δ/Klp6Δ cells ('MT_{long}', strain FY20823, see Table S1) represented in the intensity map indicated to the bottom of the images. High overpexpression of Dnm1 is indicated with '*+++*' ('WT(-thia)', and 'MT_{long}(-thia)') and low overexpression with '*++*' ('WT(+thia)', and 'MT_{long}(+thia)'). **c,** Box plot of mitochondrial numbers in WT and MT_{long} cells with high overexpression ('*+++*') or low expression of Dnm1 ('*++*') (*n*= 149, 37, 63, 41 cells respectively). The mitochondrial numbers in WT and MT_{long} cells expressing normal amount of Dnm1 ('*+*') are depicted by the dashed lines. Light grey crosses represent outliers, asterisk represents significance ($p<0.05$). **d,** Model of mitochondrial dynamics mediated by microtubule dynamics. Microtubules polymerise and depolymerise at their plus ends ('+'). Absence of microtubule bundles in the cytoplasm

during cell division enables the fragmentation of mitochondria. **e,** When mitochondria are bound to microtubules, Dnm1 ring assembly might be inhibited. Upon microtubule depolymerisation, this inhibition is alleviated and Dnm1 can effectively mediate scission of mitochondria.

To test the influence of microtubule dynamics and in essence, microtubule lengths on the fission-fusion status of mitochondria, we transformed wild-type and Klp5Δ/Klp6Δ cells with a plasmid expressing untagged Dnm1 under the control of the nmt1 promoter (see Table S1) and visualized the mitochondria (Fig. 5b). In these cells, Dnm1 shows high overexpression in the absence of thiamine and low overexpression in the presence of 0.05μM thiamine in the culture medium. We counted the number of mitochondria present in these cells and estimated that wild-type cells highly overexpressing Dnm1 exhibited 11.6 ± 0.2 mitochondria (mean ± s.e.m), which is twice that of wild-type cells expressing normal levels of Dnm1 (Fig. 5c). The increase in mitochondrial numbers in these cells is due to the increase in Dnm1 numbers, that likely accelerates the kinetics of the Dnm1 ring formation and hence, mitochondrial fission. In wild-type cells that were grown in the presence of thiamine, the mitochondrial number was 7 ± 0.3 (mean ± s.e.m.), presumably because of low overexpression of Dnm1. Interestingly, in Klp5Δ/Klp6Δ cells with high and low overexpression of Dnm1, we counted only 7.5 ± 0.3 mitochondria and 5.2 ± 0.2 mitochondria (mean ± s.e.m.) respectively. In Klp5Δ/Klp6Δ, the presence of longer microtubules than wild-type cells possibly prevented increased fission of mitochondria even when cells overexpressed Dnm1. In fact, in Klp5Δ/Klp6Δ cells where there was low overexpression of Dnm1, the mitochondrial number was comparable to that in wild-type cells expressing normal levels of Dnm1 (Fig. 5c).

Extended Data Fig. 5c contains a summary of the mitochondrial parameters measured in this study.

Discussion

We discovered that microtubule dynamics is a strong determinant for mitochondrial dynamics and thereby, morphology. Mitochondrial fission frequency was proportional to microtubule catastrophe rate. While previous studies discounted the role of motors in the determination of mitochondrial positioning in fission yeast[23,26,41,42], we have identified kinesin-like proteins that regulate mitochondrial morphology through their control over microtubule length. The distribution of mitochondrial sizes that we observed in wild-type

332 cells and cells with long and short microtubules could be explained by the allocation of the
333 same amount of mitochondria between different numbers of mitochondria. We observed the
334 maximum number of mitochondria, and thereby the smallest mitochondrial sizes, in cells
335 with short microtubules.

336 We propose that equilibrium between fission and fusion of mitochondria in
337 interphase cells can be maintained solely by the inherent dynamic instability of
338 microtubules. Perturbation of microtubule dynamics shifts the balance between fission and
339 fusion frequencies to a different set point, leading to modification of mitochondrial numbers
340 and morphology. In mammalian cells, mitochondria employ microtubule-associated
341 machinery to traverse the cell. In HeLa cells, Drp1 recruitment to the mitochondria was
342 observed to be dependent on dynein[43]. Mobile mitochondria on microtubules have also
343 been seen to participate in kiss-and-run fusions that are transient[44]. Additionally, the role of
344 microtubule-stabilizing and destabilizing drugs has been tested on the biogenesis of
345 mitochondria[45]. In taxol-treated cells, mitochondria appeared more elongated whereas in
346 nocodazole-treated cells, mitochondria seemed fragmented[45]. However, a direct role for
347 microtubule localization on mitochondrial fission has not been explored.

348 We observed that fission yeast cells fragment mitochondria by emptying the
349 cytoplasm of its microtubules upon onset of mitosis, thereby ensuring stochastic
350 partitioning[37] of the several small mitochondria between future daughter cells (Fig. 5d). The
351 increase in mitochondrial numbers prior to cell division likely serves to create a well-mixed,
352 homogeneous cytoplasm that is primed for stochastic segregation of mitochondria.
353 Mitochondrial fragmentation also reduces the partitioning error between the daughter
354 cells[38], since mitochondrial numbers of 5 or less, which is typical of wild-type interphase
355 cells, exhibit errors between ~45 and 100% (Extended Data Fig. 4d). While fission yeast
356 cells employ this strategy, mammalian cells might additionally employ motor proteins to
357 actively segregate mitochondria during cell division.

358 We observed that Dnm1 spots were excluded from microtubules. We propose the
359 failure of Dnm1 ring assembly in the presence of microtubules as the nexus between
360 microtubule dynamics and mitochondrial dynamics (Fig. 5e). Previously, cryo-electon
361 tomographic analysis in fission yeast indicated a preferred separation distance of ~20nm for
362 mitochondria associated with microtubules[46]. So too, cryo-elctron microscopy in budding
363 yeast revealed that Dnm1 assembled into rings with an outer diameter of 129nm and lumen

364 diameter of 89nm, resulting in ~40nm-high structures around mitochondria[47]. Therefore,
365 mitochondria associated with microtubules might have insufficient space to accommodate
366 the Dnm1 ring around their diameter, thereby inhibiting fission due to simple physical
367 constraints.

368 Alternatively, increased fission upon microtubule depolymerization might be brought
369 about by phosphorylation of the mitochondrial fission protein Dnm1. Mammalian Drp1
370 undergoes phosphorylation at S616 mediated by Cdk1/cyclin B during cell division and
371 increases mitochondrial fission[48]. Fission yeast Dnm1 however lacks this phosphorylation
372 site. Drp1 also contains another phosphorylation site at S637, which is conserved in Dnm1.
373 However, PKA-mediated phosphorylation at S637 has been shown to inhibit fission by
374 Drp1[49], whereas Ca+/calmodulin-dependent protein kinase α-dependent phosphorylation of
375 Drp1 S637 in rat hippocampal neurons was shown to increase fission[50]. To date, yeast
376 Dnm1 has not been demonstrated to undergo phosphorylation at this site. Future studies
377 will help delineate whether the increased fission upon microtubule depolymerization is due
378 to a simple physical impediment to the assembly of Dnm1 ring or a more complex
379 biochemical signal tethered to microtubules that changes the phosphorylation status of
380 Dnm1 to activate it.

381 We also observed that the presence of long microtubules was inhibitory for fission of
382 mitochondria even in the overexpression of the fission protein Dnm1. Wild-type cells
383 contained the same total amount of mitochondria as cells with long microtubules, but
384 exhibited increased mitochondrial fission in the presence of increased Dnm1 levels. In
385 disease states such as cancer[51] and neurodegeneration[52], mitochondrial fragmentation has
386 been linked with overexpression of Drp1 in mammalian cells. In this work, we have
387 identified that cells that present increased microtubule stabilization are able to overcome
388 the effect of Dnm1 overexpression.

389 Destabilisation of microtubules is a hallmark of several neurodegenerative disorders
390 including Alzheimer's, Parkinson's and Huntington's disease[53]. So too, colorectal cancer
391 has been characterised by the absence of the tumour suppressor gene APC, which also
392 modulates microtubule dynamics[54]. Remarkably, all these disease states have also been
393 correlated with dysfunction of mitochondrial dynamics[11,55]. In future, it would be interesting
394 to investigate the effect of restoration of microtubule dynamics on the mitochondrial fission
395 and fusion in these scenarios, and consequently on the disease states.

396 **Methods**

397 **Strains and media.** The fission yeast strains used in this study are listed in Table S1. All
398 the strains were grown in YE (yeast extract) media or Edinburg Minimal media (EMM)[56] with
399 appropriate supplements at a temperature of 30˚C. Cells that were transformed with
400 pREP41-Dnm1-Cterm-GFP or pREP41-Dnm1 (see below) were cultured in EMM with
401 appropriate supplements and 0.05μM thiamine for partial induction of the nmt1 promoter.

402 **Plasmid transformation.** Transformation of strains MTY271, FY7143, FY20823 and
403 McI438 with plasmid pREP41-Dnm1-Cterm-GFP and pREP41-Dnm1 (see Table S1) was
404 carried out using the improved protocol for rapid transformation of fission yeast[57]. In brief,
405 cells were grown overnight to log phase in low glucose EMM, pelleted and washed with
406 distilled water. The cells were then washed in a solution of lithium acetate/EDTA (100mM
407 LiAc, 1mM EDTA, pH 4.9) and re-suspended in the same solution. 1μg of plasmid DNA was
408 added to the suspension, followed by addition of lithium acetate/PEG (40% w/v PEG,
409 100mM LiAc, 1mM EDTA, pH 4.9) and then incubated at 30°C for 30 min. This was
410 followed by a heat shock of 15min at 42°C. Thereafter, cells were pelleted down, re-
411 suspended in TE solution (10mM Tris-HCl, 1mM EDTA, pH 7.5) and plated onto selective
412 EMM plates.

413 **Preparation of yeast for imaging.** For imaging mitochondria, fission yeast cells were
414 grown overnight in a shaking incubator at 30°C, washed once with distilled water, and
415 stained with 200nM Mitotracker Orange CMTMRos (ThermoFisher Scientific, Cat. #M7510)
416 dissolved in EMM for 20min. Following this, cells were washed thrice with EMM and then
417 allowed to adhere on lectin-coated (Sigma-Aldrich, St. Louis, MO, Cat. #L2380) 35mm
418 confocal dishes (SPL, Cat. #100350) for 20min. Unattached cells were then removed by
419 washing with EMM. In experiments where mitochondria were not imaged, staining with
420 Mitotracker was omitted.

421 **Microtubule depolymerisation.** For depolymerisation of microtubules, cells were treated
422 with methyl benzimidazol-2-yl-carbamate (MBC, Carbendazim 97%, Sigma Aldrich). A
423 stock solution with a concentration of 25mg/ml was prepared in DMSO and later diluted to a
424 working concentration of 25μg/ml in EMM.

425 **Microscopy.** Confocal microscopy was carried out using the InCell Analyzer-6000 (GE
426 Healthcare, Buckinghamshire, UK) with 60x/0.7 N.A. objective fitted with an sCMOS 5.5MP
427 camera having an x-y pixel separation of 108nm. For GFP and Mitotracker Orange imaging,
428 488 and 561nm laser lines and bandpass emission filters 525/20 and 605/52nm

429 respectively were employed. Time-lapses for visualisation of mitochondrial dynamics were
430 captured by obtaining 5 Z-stacks with a 0.5μm-step size every 12s. Deconvolution was
431 performed in images obtained using a Deltavision RT microscope (Applied Precision) with a
432 100×, oil-immersion 1.4 N.A. objective (Olympus, Japan). Excitation of fluorophores was
433 achieved using InsightSSI (Applied Precision) and corresponding filter selection for
434 excitation and emission of GFP and Mitotracker Orange. Z-stacks with 0.3μm-step sizes
435 encompassing the entire cell were captured using a CoolSnapHQ camera (Photometrics),
436 with 2X2 binning. The system was controlled using softWoRx 3.5.1 software (Applied
437 Precision) and the deconvolved images obtained using the built-in setting for each channel.
438 **3D visualisation of deconvolved images**. 3D views of the microtubules and mitochondria
439 in Supplementary Movies S2, S3, S4, S8, S9 and S10 were obtained from deconvolved
440 images captured in the Deltavision microscope using Fiji's '3D project' function, with the
441 brightest point projection method and 360˚ total rotation with 10˚ rotation angle increment.
442 **Estimation of volume of mitochondria.** Mitochondrial volume was estimated in Fiji by
443 integrating the areas of mitochondria in thresholded 3D stacks of cells in fluorescent
444 deconvolved images obtained using the Deltavision RT microscope. The total volume was
445 then normalised to the mean total mitochondrial volume of wild-type cells. Individual
446 mitochondrial volumes were estimated in the same fashion.
447 **Analysis of mitochondrial dynamics.** Individual mitochondria were identified in each
448 frame of the time-lapse obtained in confocal mode of the GE InCell Analyzer after projecting
449 the maximum intensity of the 3D stack encompassing the cell, followed by mean filtering
450 and visualisation in Fiji's 'mpl-magma' lookup table. Following identification of mitochondria,
451 the 'Measure' function of Fiji was employed to obtain the circularity, aspect ratio and
452 parameters of fitted ellipse. The length of the major axis of the ellipse fitted to a
453 mitochondrion was defined as the size of that mitochondrion. The size, circularity and
454 aspect ratio were estimated for mitochondria at each frame and each time point. Fission
455 and fusion frequencies of mitochondria were estimated by counting the number of
456 mitochondria identified during each frame of the time-lapse. The difference in number of
457 mitochondria from one frame to the next was counted, with an increase being counted as
458 fission event and decrease as fusion event. The total number of fission events and fusion
459 events per cell were estimated and divided by the total duration of the time-lapse to obtain
460 the fission and fusion frequencies.

Simulation of mitochondrial size distribution. Mitochondrial size distributions in wild-type, Klp5Δ/Klp6Δ and Klp4Δ cells were simulated by taking experimentally measured mitochondrial numbers in the three cases and assuming that the total mitochondrial amount was the same. Briefly, to make the system amenable to simulation using an integer-partitioning problem, the total mitochondrial amount was taken to be a constant of 10. The minimum size of mitochondria that could be present was assumed to be 1. The total mitochondria was then partitioned between the available mitochondrial numbers in wild-type, Klp5Δ/Klp6Δ and Klp4Δ cells of ~4, ~2 and ~7 in units of 1. The distributions were then normalised to total mitochondrial amount to get mitochondrial sizes as fractions of the total mitochondrial content. The minimum mitochondrial size thus obtained in this case, 0.1, is similar to experimentally obtained normalised minimum mitochondrial sizes.

Test for fit of mitochondrial partitioning during mitosis to binomial distribution. To test the fit of mitochondrial segregation during mitosis to a binomial distribution, the data were z-transformed as previously described[38]. Briefly, given n mitochondria in the mother cell just prior to cell division, x and $n - x$ mitochondria in the resulting daughter cells, z was given by $2x - n/\sqrt{n}$ to approximate the binomial distribution to a normal distribution of 0,1. The z values obtained for each x and n were binned into k bins of equal sizes and subjected to Chi-square test with $k - 1$ degrees of freedom. The z values are expected to be equally distributed among the k bins, with expected number of $1/k$ per bin.

Data analysis and plotting. Data analysis was performed in Matlab (Mathworks, Natick, MA). Box plots with the central line indicating the median and notches that represent the 95% confidence interval of the median were obtained by performing one-way ANOVA ('anova1' in Matlab). Following this, significance ($p<0.05$) of the means was tested using the Tukey-Kramer post-hoc test. All the plots were generated using Matlab.

References

1. Smirnova, E., Griparic, L., Shurland, D. L. & van der Bliek, A. M. Dynamin-related protein Drp1 is required for mitochondrial division in mammalian cells. *Mol. Biol. Cell* **12,** 2245–56 (2001).
2. Bleazard, W. *et al.* The dynamin-related GTPase Dnm1 regulates mitochondrial fission in yeast. *Nat. Cell Biol.* **1,** 298–304 (1999).
3. Jourdain, I., Gachet, Y. & Hyams, J. S. The dynamin related protein Dnm1 fragments mitochondria in a microtubule-dependent manner during the fission yeast cell cycle. *Cell Motil. Cytoskeleton* **66,** 509–523 (2009).
4. Ingerman, E. *et al.* Dnm1 forms spirals that are structurally tailored to fit mitochondria.

496 *J. Cell Biol.* **170,** 1021–7 (2005).
497 5. Basu, K. *et al.* Molecular mechanism of DRP1 assembly studied in vitro by cryo-
498 electron microscopy. *PLoS One* **12,** e0179397 (2017).
499 6. Delettre, C. *et al.* Nuclear gene OPA1, encoding a mitochondrial dynamin-related
500 protein, is mutated in dominant optic atrophy. *Nat. Genet.* **26,** 207–210 (2000).
501 7. Sesaki, H., Southard, S. M., Yaffe, M. P. & Jensen, R. E. Mgm1p, a dynamin-related
502 GTPase, is essential for fusion of the mitochondrial outer membrane. *Mol. Biol. Cell*
503 **14,** 2342–56 (2003).
504 8. Eura, Y., Ishihara, N., Yokota, S. & Mihara, K. Two Mitofusin Proteins, Mammalian
505 Homologues of FZO, with Distinct Functions Are Both Required for Mitochondrial
506 Fusion. *J. Biochem.* **134,** 333–344 (2003).
507 9. Hermann, G. J. *et al.* Mitochondrial fusion in yeast requires the transmembrane
508 GTPase Fzo1p. *J. Cell Biol.* **143,** 359–73 (1998).
509 10. Mishra, P. & Chan, D. C. Metabolic regulation of mitochondrial dynamics. *J. Cell Biol.*
510 **212,** 379–87 (2016).
511 11. Chen, H. & Chan, D. C. Mitochondrial dynamics--fusion, fission, movement, and
512 mitophagy--in neurodegenerative diseases. *Hum. Mol. Genet.* **18,** R169-76 (2009).
513 12. Hirai, K. *et al.* Mitochondrial abnormalities in Alzheimer's disease. *J. Neurosci.* **21,**
514 3017–23 (2001).
515 13. Deng, H., Dodson, M. W., Huang, H. & Guo, M. The Parkinson's disease genes pink1
516 and parkin promote mitochondrial fission and/or inhibit fusion in Drosophila. *Proc.*
517 *Natl. Acad. Sci.* **105,** 14503–14508 (2008).
518 14. Graves, J. A. *et al.* Mitochondrial Structure, Function and Dynamics Are Temporally
519 Controlled by c-Myc. *PLoS One* **7,** e37699 (2012).
520 15. Ashrafian, H. *et al.* A Mutation in the Mitochondrial Fission Gene Dnm1l Leads to
521 Cardiomyopathy. *PLoS Genet.* **6,** e1001000 (2010).
522 16. Pilling, A. D., Horiuchi, D., Lively, C. M. & Saxton, W. M. Kinesin-1 and Dynein are the
523 primary motors for fast transport of mitochondria in Drosophila motor axons. *Mol. Biol.*
524 *Cell* **17,** 2057–68 (2006).
525 17. Stowers, R. S., Megeath, L. J., Górska-Andrzejak, J., Meinertzhagen, I. A. &
526 Schwarz, T. L. Axonal transport of mitochondria to synapses depends on milton, a
527 novel Drosophila protein. *Neuron* **36,** 1063–77 (2002).
528 18. Glater, E. E., Megeath, L. J., Stowers, R. S. & Schwarz, T. L. Axonal transport of
529 mitochondria requires milton to recruit kinesin heavy chain and is light chain
530 independent. *J. Cell Biol.* **173,** 545–57 (2006).
531 19. van Spronsen, M. *et al.* TRAK/Milton Motor-Adaptor Proteins Steer Mitochondrial
532 Trafficking to Axons and Dendrites. *Neuron* **77,** 485–502 (2013).
533 20. Chen, Y. & Sheng, Z.-H. Kinesin-1-syntaphilin coupling mediates activity-dependent
534 regulation of axonal mitochondrial transport. *J. Cell Biol.* **202,** 351–64 (2013).
535 21. Kang, J.-S. *et al.* Docking of Axonal Mitochondria by Syntaphilin Controls Their
536 Mobility and Affects Short-Term Facilitation. *Cell* **132,** 137–148 (2008).
537 22. Fu, C., Jain, D., Costa, J., Velve-Casquillas, G. & Tran, P. T. Mmb1p binds
538 mitochondria to dynamic microtubules. *Curr. Biol.* **21,** 1431–1439 (2011).
539 23. Li, T., Zheng, F., Cheung, M., Wang, F. & Fu, C. Fission yeast mitochondria are
540 distributed by dynamic microtubules in a motor-independent manner. *Sci. Rep.* **5,**
541 11023 (2015).
542 24. Huh, D. & Paulsson, J. Random partitioning of molecules at cell division. *Proc. Natl.*
543 *Acad. Sci. U. S. A.* **108,** 15004–9 (2011).

544 25. Lawrence, E. & Mandato, C. Mitochondrial inheritance is mediated by microtubules in
545 mammalian cell division. *Commun. Integr. Biol.* **6,** e27557 (2013).
546 26. Yaffe, M. P., Stuurman, N. & Vale, R. D. Mitochondrial positioning in fission yeast is
547 driven by association with dynamic microtubules and mitotic spindle poles. *PNAS*
548 **100,** 11424–11428 (2003).
549 27. Krüger, N. & Tolic, I. M. Association of mitochondria with spindle poles facilitates
550 spindle alignment. *Curr. Biol.* **18,** 646–647 (2008).
551 28. Bergeland, T., Widerberg, J., Bakke, O. & Nordeng, T. W. Mitotic partitioning of
552 endosomes and lysosomes. *Curr. Biol.* **11,** 644–651 (2001).
553 29. Shima, D. T., Cabrera-Poch, N., Pepperkok, R. & Warren, G. An ordered inheritance
554 strategy for the Golgi apparatus: visualization of mitotic disassembly reveals a role for
555 the mitotic spindle. *J. Cell Biol.* **141,** 955–66 (1998).
556 30. Tischer, C., Brunner, D. & Dogterom, M. Force- and kinesin-8-dependent effects in
557 the spatial regulation of fission yeast microtubule dynamics. *Mol. Syst. Biol.* **5,** 250
558 (2009).
559 31. West, R. R., Malmstrom, T., Troxell, C. L. & McIntosh, J. R. Two related kinesins,
560 klp5+ and klp6+, foster microtubule disassembly and are required for meiosis in
561 fission yeast. *Mol. Biol. Cell* **12,** 3919–32 (2001).
562 32. Browning, H. *et al.* Tea2p is a kinesin-like protein required to generate polarized
563 growth in fission yeast. *J. Cell Biol.* **151,** 15–28 (2000).
564 33. Busch, K. E., Hayles, J., Nurse, P. & Brunner, D. Tea2p Kinesin Is Involved in Spatial
565 Microtubule Organization by Transporting Tip1p on Microtubules. *Dev. Cell* **6,** 831–
566 843 (2004).
567 34. Beinhauer, J. D., Hagan, I. M., Hegemann, J. H. & Fleig, U. Mal3, the fission yeast
568 homologue of the human APC-interacting protein EB-1 is required for microtubule
569 integrity and the maintenance of cell form. *J. Cell Biol.* **139,** 717–28 (1997).
570 35. Pletjushkina, O. Y. *et al.* Effect of oxidative stress on dynamics of mitochondrial
571 reticulum. *Biochim. Biophys. Acta - Bioenerg.* **1757,** 518–524 (2006).
572 36. Ding, R., West, R. R., Morphew, D. M., Oakley, B. R. & McIntosh, J. R. The spindle
573 pole body of Schizosaccharomyces pombe enters and leaves the nuclear envelope
574 as the cell cycle proceeds. *Mol. Biol. Cell* **8,** 1461–79 (1997).
575 37. Birky, C. W. The partitioning of cytoplasmic organelles at cell division. *Int. Rev. Cytol.*
576 *Suppl.* **15,** 49–89 (1983).
577 38. Hennis, A. S. & Birky, C. W. Stochastic partitioning of chloroplasts at cell division in
578 the alga Olisthodiscus, and compensating control of chloroplast replication. *J. Cell*
579 *Sci.* **70,** 1–15 (1984).
580 39. Guillou, E., Bousquet, C., Daloyau, M., Emorine, L. J. & Belenguer, P. Msp1p is an
581 intermembrane space dynamin-related protein that mediates mitochondrial fusion in a
582 Dnm1p-dependent manner in S. pombe. *FEBS Lett.* **579,** 1109–16 (2005).
583 40. Maundrell, K. nmt1 of fission yeast. A highly transcribed gene completely repressed
584 by thiamine. *J. Biol. Chem.* **265,** 10857–64 (1990).
585 41. Brazer, S. W., Williams, H. P. & Chappell, T. G. A fission yeast kinesin affects Golgi
586 membrane recycling. 149–166 (2000).
587 42. Chiron, S., Bobkova, A., Zhou, H. & Yaffe, M. P. CLASP regulates mitochondrial
588 distribution in Schizosaccharomyces pombe. *J. Cell Biol.* **182,** 41–49 (2008).
589 43. Varadi, A. *et al.* Cytoplasmic dynein regulates the subcellular distribution of
590 mitochondria by controlling the recruitment of the fission factor dynamin-related
591 protein-1. *J. Cell Sci.* **117,** 4389–400 (2004).

44. Liu, X., Weaver, D., Shirihai, O. & Hajnóczky, G. Mitochondrial 'kiss-and-run': interplay between mitochondrial motility and fusion-fission dynamics. *EMBO J.* **28,** 3074–89 (2009).
45. Karbowski, M. *et al.* Opposite effects of microtubule-stabilizing and microtubule-destabilizing drugs on biogenesis of mitochondria in mammalian cells. *J. Cell Sci.* **114,** 281–291 (2001).
46. Höög, J. L. *et al.* Organization of interphase microtubules in fission yeast analyzed by electron tomography. *Dev. Cell* **12,** 349–61 (2007).
47. Mears, J. A. *et al.* Conformational changes in Dnm1 support a contractile mechanism for mitochondrial fission. *Nat. Struct. Mol. Biol.* **18,** 20–26 (2011).
48. Taguchi, N., Ishihara, N., Jofuku, A., Oka, T. & Mihara, K. Mitotic phosphorylation of dynamin-related GTPase Drp1 participates in mitochondrial fission. *J. Biol. Chem.* **282,** 11521–9 (2007).
49. Chang, C.-R. & Blackstone, C. Cyclic AMP-dependent protein kinase phosphorylation of Drp1 regulates its GTPase activity and mitochondrial morphology. *J. Biol. Chem.* **282,** 21583–7 (2007).
50. Han, X.-J. *et al.* CaM kinase Iα–induced phosphorylation of Drp1 regulates mitochondrial morphology. *J. Cell Biol.* **182,** 573–585 (2008).
51. Ferreira-da-Silva, A. *et al.* Mitochondrial Dynamics Protein Drp1 Is Overexpressed in Oncocytic Thyroid Tumors and Regulates Cancer Cell Migration. *PLoS One* **10,** e0122308 (2015).
52. Itoh, K., Nakamura, K., Iijima, M. & Sesaki, H. Mitochondrial dynamics in neurodegeneration. *Trends Cell Biol.* **23,** 64–71 (2013).
53. Dubey, J., Ratnakaran, N. & Koushika, S. P. Neurodegeneration and microtubule dynamics: death by a thousand cuts. *Front. Cell. Neurosci.* **9,** 343 (2015).
54. Kroboth, K. *et al.* Lack of Adenomatous Polyposis Coli Protein Correlates with a Decrease in Cell Migration and Overall Changes in Microtubule Stability. *Mol. Biol. Cell* **18,** 910–918 (2007).
55. Senft, D. & Ronai, Z. A. Regulators of mitochondrial dynamics in cancer. *Curr. Opin. Cell Biol.* **39,** 43–52 (2016).
56. Forsburg, S. L. & Rhind, N. Basic methods for fission yeast. *Yeast* **23,** 173–183 (2006).
57. Kanter-Smoler, G., Dahlkvist, A. & Sunnerhagen. Improved Method for rapid Transformation of Intact Schizosaccharomyces pombe cells. *Biotechniques* **16,** 798–800 (1994).

Acknowledgements

We thank J. M. Thankachan, S. S. Nuthalapati and M. Ayushman for pilot experiments; High Content Imaging Facility at BSSE, IISc, and P. I. Rajyaguru for the use of the InCell 6000, and Deltavision RT microscopes respectively; P. Delivani, I. Jourdain, R.C. Salas, M. Takaine, I. Tolic, P. Tran, and NBRP Japan for yeast strains and constructs; S. Jain for CellROX reagent. The research was supported by the Department of Science and Technology (India)-INSPIRE Faculty Award, the Department of Biotechnology (India) Innovative Young Biotechnologist Award, and the Science and Engineering Research

Board (SERB, India) Early Career Research Award awarded to V.A., and SERB Early Career Research Award awarded to S.J.

Author Contributions

K.M. carried out the Dnm1 experiments, M.K.C. and S. J. carried out and analysed the flow cytometry experiments, V.A. performed all the other experiments and data analysis, designed the project, and wrote the paper.

Competing Financial Interests

The authors declare no competing financial interests.

Extended Data

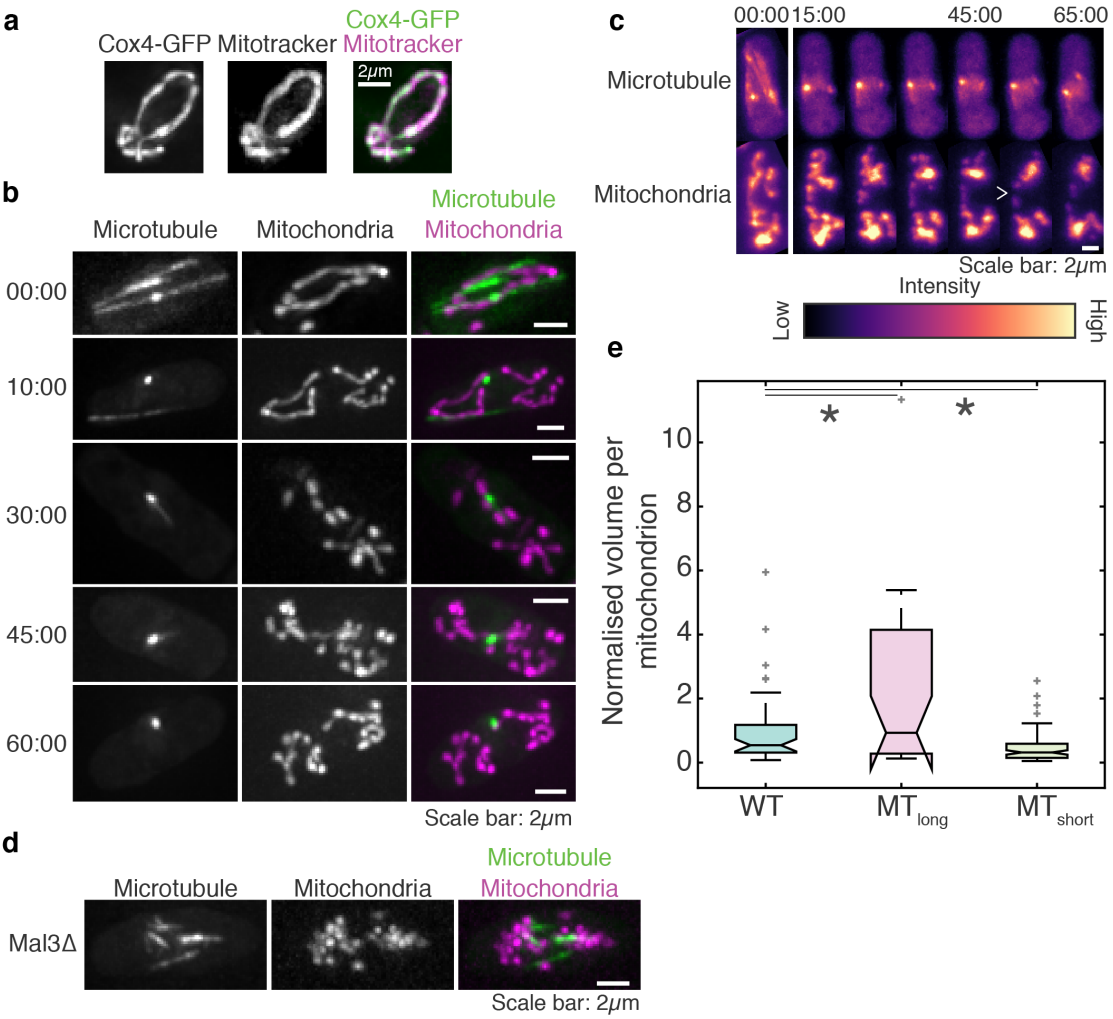

Extended Data Figure 1. Depolymerisation of microtubules increases mitochondrial fission. a, Maximum intensity projections of deconvolved Z-stack images of Cox4-GFP (left), Mitotracker Orange staining (centre) and their composite (right) in interphase cells (strain PT.1650, see Table S1) showing colocalisation of both signal intensities. **b,** Maximum intensity projections of deconvolved Z-stack images of microtubules (left), mitochondria (centre) and their composite (right) in fission yeast cells at the onset of mitosis. Time in mm:ss is indicated to the left of the images. **c,** Montage of maximum intensity projected confocal Z-stack images of microtubule depolymerisation (top) and mitochondria (bottom) of wild-type cells (strain KI001, see Table S1) treated with MBC (see Methods) represented in the intensity map indicated at the bottom of the images. The open white arrowhead indicates a representative fission event. **d,** Box plot of the volume of individual mitochondria in wild-type ('WT'), Klp5Δ/Klp6Δ ('MT_{long}') and Klp4Δ ('MT_{short}') cells normalised to mean mitochondrial volume in wild-type cells (n=49, 28 and 100 mitochondria respectively). Light grey crosses represent outliers, asterisk represents significance ($p<0.05$) and 'n.s.' indicates no significant difference. **e,** Maximum intensity projections of deconvolved Z-stack images of microtubule (left), mitochondria (centre) and their composite (right) in interphase Mal3Δ cells (strain KN001, see Table S1) showing several small mitochondrial fragments similar to those seen in Klp4Δ cells.

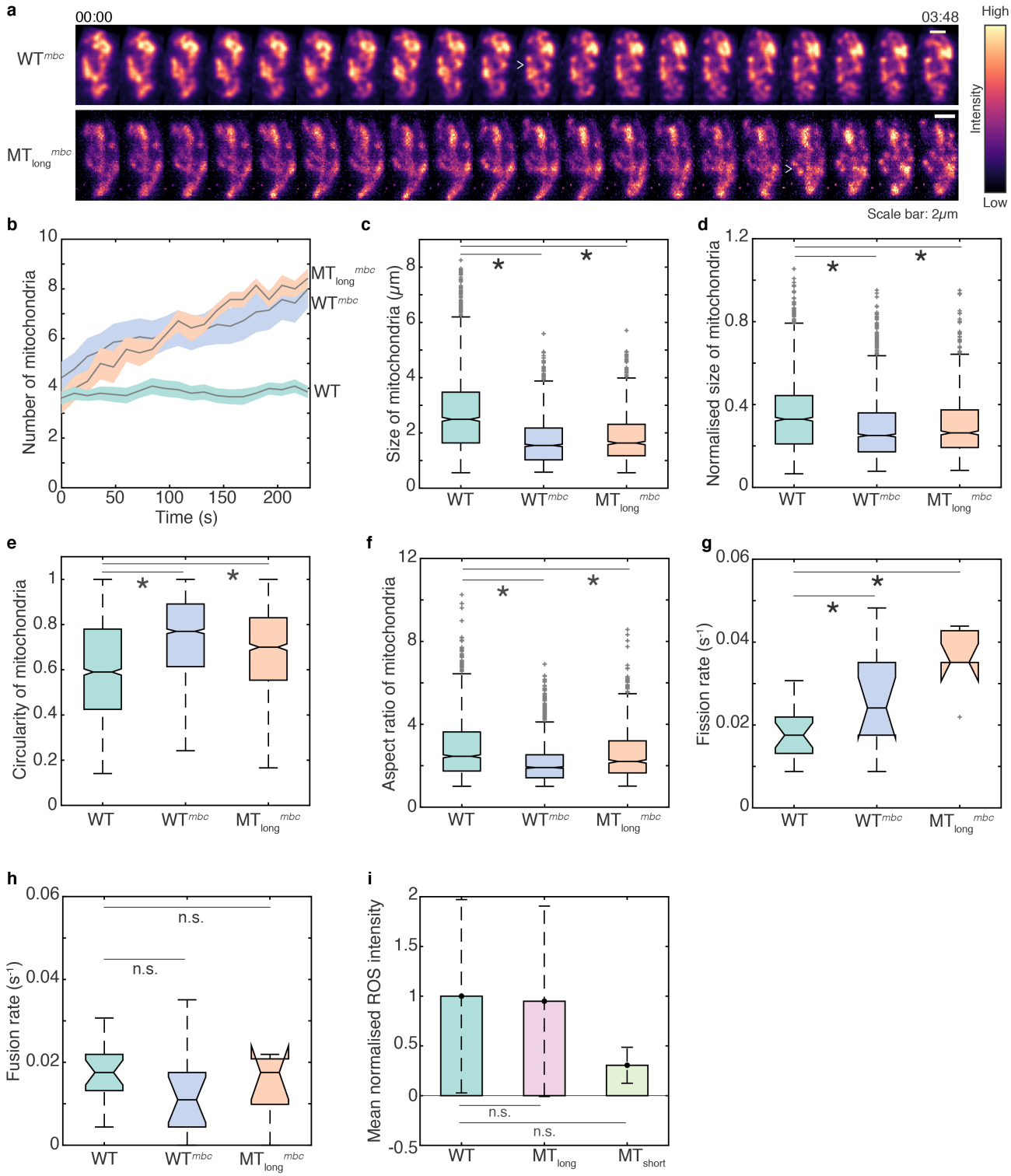

Extended Data Figure 2. Microtubule depolymerisation induces increased fission in Klp5Δ/Klp6Δ cells. a, Montage of maximum intensity projected confocal Z-stack images of MBC-treated wild-type (WT^{mbc}, strain KI001, see Table S1) and Klp5Δ/Klp6Δ ('MT_{long}^{mbc}', strain G3B, see Table S1) cells represented in the intensity map indicated to the right of the images. White open arrowheads point to representative fission events. 00:00 indicates time (mm:ss) 2min after addition of MBC. **b,** Evolution of mitochondrial number with time indicated as mean (solid grey line) and standard error of the mean (shaded region) for wild-type ('WT'), WT^{mbc}, and MT_{long}^{mbc} cells (*n*=21, 14 and 7 cells respectively). **c,** Box plot of the size of mitochondria in WT, WT^{mbc}, and MT_{long}^{mbc} cells, calculated as the length of the major

axis of an ellipse fitted to each mitochondrion (*n*=1613, 1765 and 886 mitochondria respectively). **d,** Box plot of the size of individual mitochondria in WT, WT^{mbc}, and MT_{long}^{mbc} cells normalised to their cell lengths (*n*=1613, 1765 and 886 mitochondria respectively). **e,** Box plot of the circularity of mitochondria in WT, WT^{mbc}, and MT_{long}^{mbc} cells (*n*=1613, 1765 and 886 mitochondria respectively). **f,** Box plot of the aspect ratio of mitochondria in WT, WT^{mbc}, and MT_{long}^{mbc} cells (*n*=1613, 1765 and 886 mitochondria respectively). **g,** Box plot of the fission frequencyof mitochondria per second in WT, WT^{mbc}, and MT_{long}^{mbc} cells (*n*=21, 14 and 7 cells respectively). **h,** Box plot of the fusion frequencyof mitochondria per second in WT, WT^{mbc}, and MT_{long}^{mbc} cells (*n*=21, 14 and 7 cells respectively). **i,** Bar plot of cellular ROS measured using flow cytometry (see Supplementary Information) in live WT, MT_{long} and MT_{short} cells normalised to mean of the ROS intensity in WT cells (*n*=3 independent experiments, ≥10,000 events each). Light grey crosses represent outliers, asterisk represents significance ($p<0.05$) and 'n.s.' indicates no significant difference. Note that the WT data represented in this figure is the identical to the wild-type data plotted in Fig. 2 and Extended Data Fig. 2 and has been re-used for comparison.

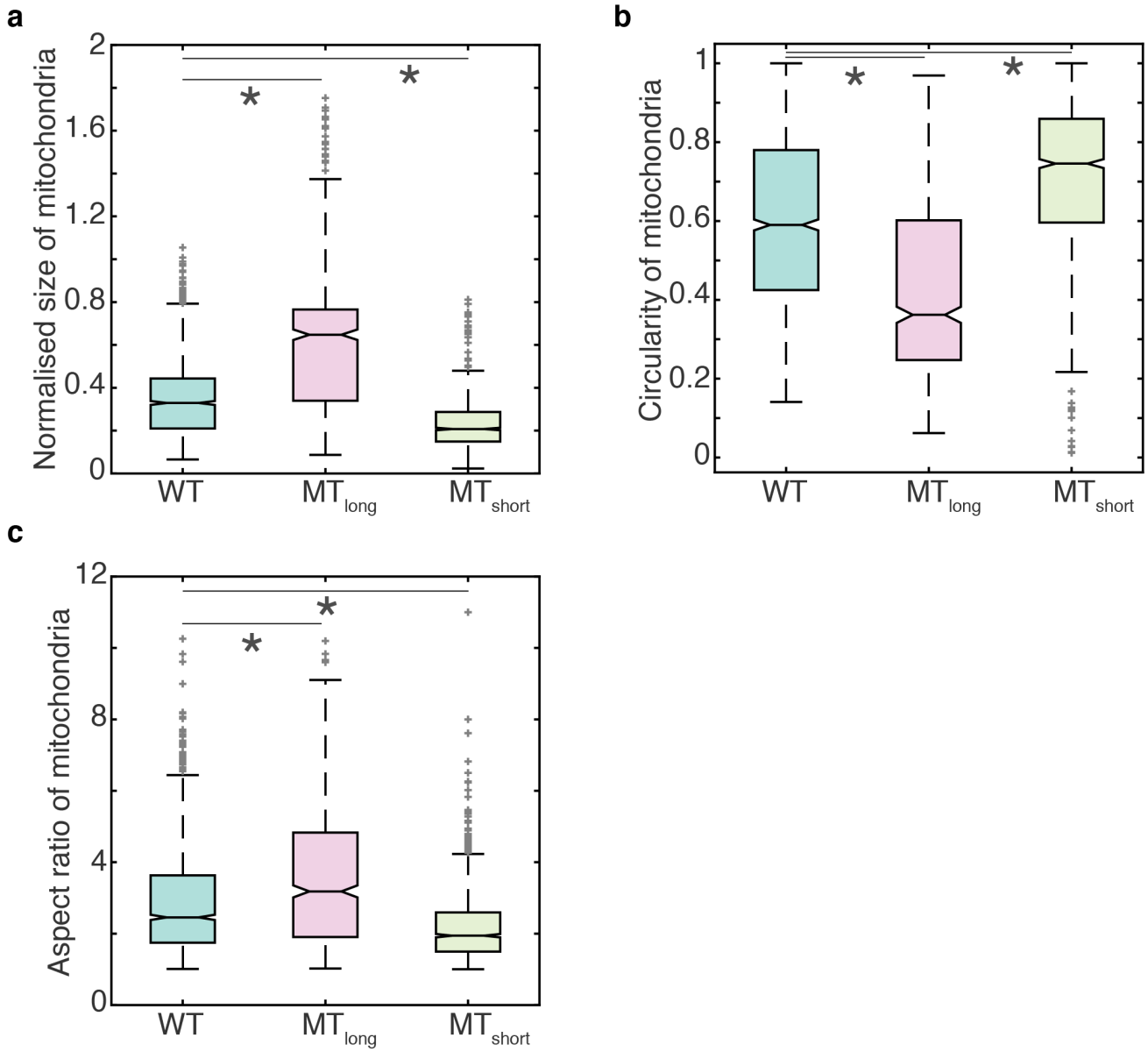

692
693 **Extended Data Figure 3. Microtubule dynamics determines the morphology of**
694 **mitochondria. a,** Box plot of the size of individual mitochondria in wild-type ('WT'),
695 Klp5Δ/Klp6Δ ('MT_{long}') and Klp4Δ ('MT_{short}') cells normalised to their cell lengths (*n*=1613,
696 739 and 1326 mitochondria respectively). **b,** Box plot of the circularity of mitochondria in
697 WT, MT_{long} and MT_{short} cells (*n*=1613, 739 and 1326 mitochondria respectively). **c,** Box plot
698 of the aspect ratio of mitochondria in WT, MT_{long} and MT_{short} cells (*n*=1613, 739 and 1326
699 mitochondria respectively). Error bars represent standard deviation. Light grey crosses
700 represent outliers, asterisk represents significance ($p<0.05$) and 'n.s.' indicates no
701 significant difference.

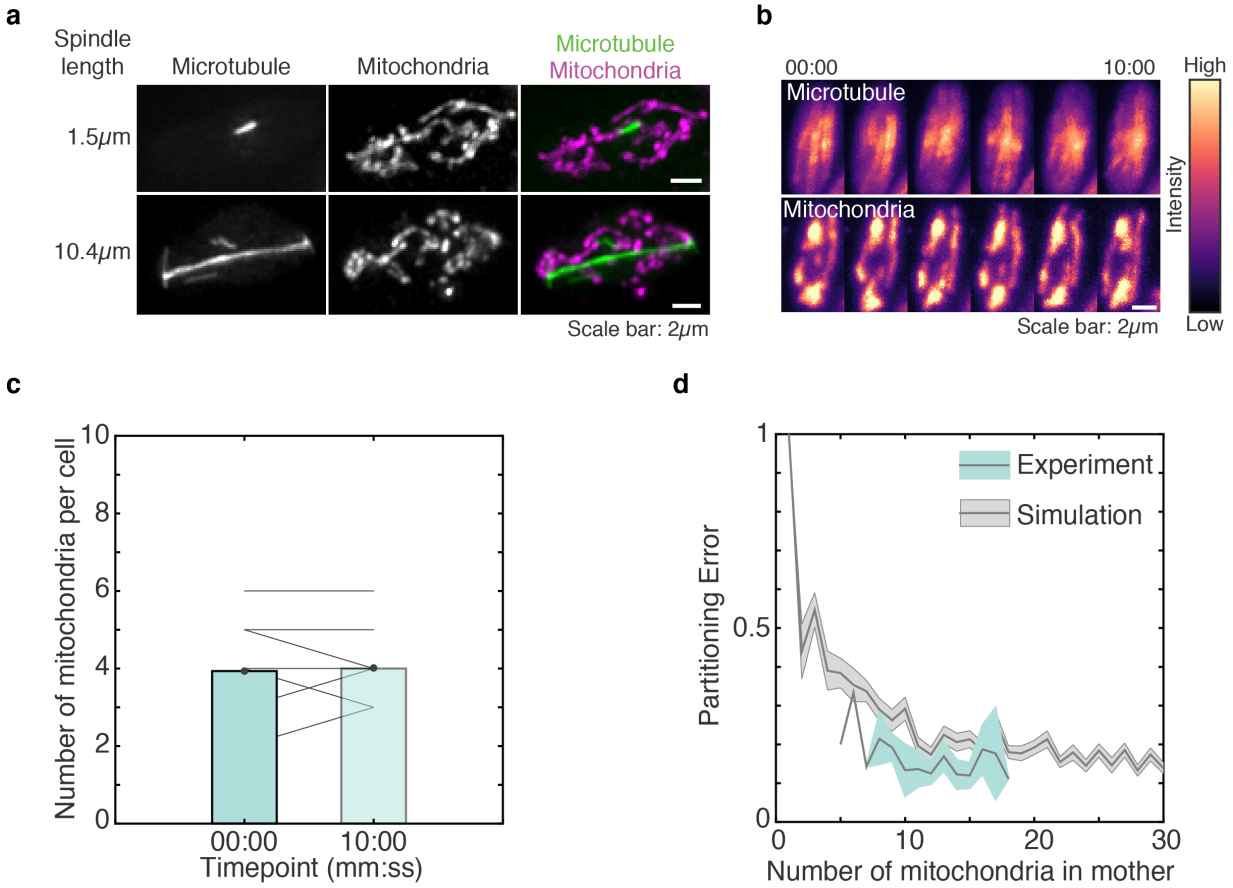

Extended Data Figure 4. Mitotic spindle length does not influence number of mitochondria. a, Maximum intensity projections of deconvolved Z-stack images of the microtubules (left), mitochondria (centre) and their composite (right) of WT cells (strain KI001, see Table S1) with short (top) and long (bottom) mitotic spindles. The length of the spindle is indicated to the left of the images. **b,** Montage of maximum intensity projected confocal Z-stack images of the microtubules (top) and mitochondria (bottom) in a non-mitotic wild-type cell (strain KI001, see Table S1) represented in the intensity map indicated to the right of the images.. **c,** Bar plot of the mean number of mitochondria per cell before ('00:00') and after ('10:00') the same time window for which mitotic cells were monitored in Fig. 3c, d. Solid grey lines represent data from individual cells (*n*=7 cells). **d,** Plot of number of mitochondria in mother cell vs. partitioning error (see Supplementary Information) between daughter cells in simulation (grey) and experiments (blue) expressed as mean (solid grey line) and standard error of the mean (shaded area).

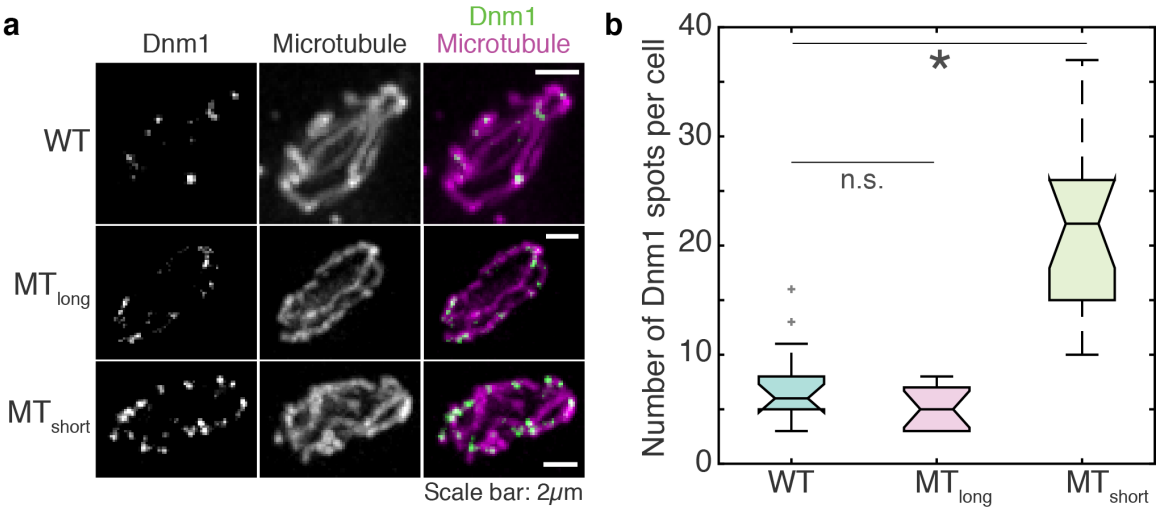

c

Parameter	Value (mean ± s.e.m)		
	WT	MT_{long}	MT_{short}
Number of mitochondria	4.9 ± 0.4	2.3 ± 0.4	10 ± 0.9
Normalised total volume of mitochondria	1.00 ± 0.10	1.09 ± 0.13	0.92 ± 0.07
Normalised volume of individual mitochondria	1.00 ± 0.16	2.30 ± 0.50	0.45 ± 0.04
Size of mitochondria (μm)	2.72 ± 0.03	6.53 ± 0.11	1.77 ± 0.02
Size of mitochondria normalised to cell length	0.35 ± 0.01	0.59 ± 0.01	0.23 ± 0.01
Circularity of mitochondria	0.60 ± 0.01	0.44 ± 0.01	0.71 ± 0.01
Aspect ratio of mitochondria	2.84 ± 0.04	3.55 ± 0.07	2.16 ± 0.03
Mitochondrial fission frequency (s^{-1})	0.018 ± 0.002	0.006 ± 0.001	0.032 ± 0.005
Mitochondrial fusion frequency (s^{-1})	0.017 ± 0.002	0.011 ± 0.001	0.025 ± 0.005

Extended Data Figure 5. Dnm1 spots colocalise with the mitochondria and their number is inversely proportional to the length of microtubules. a, Maximum intensity projections of deconvolved Z-stack images of Dnm1 (left), microtubules (centre) and their composite (right) in wild-type ('WT', strain FY7143 transformed with pREP41-Dnm1-Cterm-GFP, see Table S1), Klp5Δ/Klp6Δ ('MT_{long}', strain FY20823 transformed with pREP41-Dnm1-Cterm-GFP, see Table S1) and Klp4Δ ('MT_{short}', strain Mcl438 transformed with pREP41-Dnm1-Cterm-GFP, see Table S1) cells. **b,** Box plot of the number of Dnm1 spots in WT, MT_{long} and MT_{short} cells (n=13, 14, and 18 cells respectively). Note that the mitochondrial morphology in WT, MT_{long} and MT_{short} cells appears abnormal due to inactivity of the GFP-tagged Dnm1. Light grey crosses represent outliers, asterisk represents significance ($p<0.05$) and 'n.s.' indicates no significant difference **c,** Measured parameters relating to mitochondrial numbers and morphology in WT, MT_{long} and MT_{short} interphase cells represented as mean ± s.e.m.

731 **Supplementary Information**

732

733 **Methods**

734 **ROS detection and viability assay using flow cytometry.** A loopful of L972, FY20823 or
735 McI438 cells were inoculated in liquid YE and incubated overnight at 30°C in a shaking
736 incubator. Cells were harvested using a table-top centrifuge (2000g, 30s) and washed three
737 times with 1X PBS. The pellets were re-suspended in 500μl of 1X PBS, containing CellROX
738 (5μM) dye (ThermoFisher, USA). Following incubation at 30°C for 30min, cells were
739 washed three times with 1X PBS. Finally, cell pellets were re-suspended in an appropriate
740 volume of 1X PBS containing propidium iodide (6μg/ml), incubated for 10min at room
741 temperature, and run on a flow cytometer (BD FACS-Celesta). A minimum of 10,000 events
742 of cells was collected, and data analyzed using FlowJo (FlowJo LLC, USA). ROS was
743 reported as median fluorescence intensity for each dataset.

744 **Estimation of partitioning error during cell division.** The partitioning error of
745 mitochondria at cell division between the daughter cells Q_x was calculated from the
746 equation[24]:

$$Q_x^2 = \frac{(L-R)^2}{x^2}$$

747 where L and R were mitochondrial numbers in the resulting daughter cells and x, the
748 number of mitochondria in the mother cell. The data in Extended Data Fig. 4d were
749 simulated by independently assigning x mitochondria with 50% probability to either
750 daughter cell. Simulations were re-run 50 times to obtain the mean and the standard error
751 of the mean depicted in Extended Data Fig. 4d.

752 **Counting of Dnm1 spots.** Dnm1 was visualised in cells grown in the presence of 0.05μM
753 thiamine for partial induction of the nmt1 promoter. Even with only partial induction, a
754 majority of the cells showed extremely high expression of Dnm1, with most of the signal
755 concentrated in a single spot in the cell. The rest of the cells showed lower expression, with
756 Dnm1 signal distributed in a few spots across the cell. The latter were chosen for analysis
757 of number of Dnm1 spots. For counting the number of Dnm1 spots in Extended Data Fig.
758 5b, the maximum intensity projection of deconvolved Z-stack images were used. For
759 identification of spots, we set the lower threshold as 60-80% of the maximum intensity in
760 these images. The contrast in the images in Fig. 5a and Extended Fig. 5a reflect these
761 threshold settings.

762 **Table S1**

763

764 **Strains and constructs used in this study**

Name	Phenotype	Source
FY20823	*h- leu1 ura4 his7 Δklp5::ura4+ Δklp6::ura4+*	NBRP, Japan
FY7143	*h- ura4-D18 leu1-32 ade6-M216 his7-366*	Iva Tolić, Croatia
G3B	*h- Δklp5- Δklp6 – nmt1-GFP-atb2 leu ade*	Rafael Carazo Salas, UK
G5B	*h- klp4::kanr nmt1-GFP-atb2 leu ura*	Rafael Carazo Salas, UK
KI001	*h+ sid4-GFP::kanr kanr -nmtP3-GFP-atb2+ nmt1-pCOX4RFP::leu1+ ura4-D18 ade6-M210*	Iva Tolić, Croatia
KN001	*h + Δmal3::his3+ nmt1-pCOX4-dsRed ::leu1+ nmt1-atb1-GFP:LEU2 ade6-M210 ura4-D18 leu1-32 his3D1*	Iva Tolić, Croatia
L972	*h- WT*	Iva Tolić, Croatia
McI438	*h+ tea2d:his3 ade6 leu1-32 ura4-D18 his3-D1*	Iva Tolić, Croatia
MTY271	*h- mCherry-atb2:hphMX6 leu1-32 ura-d18*	Masakatsu Takaine, Japan
PT1650	*h+ cox4-GFP:leu1 ade6-M210 leu1-32 ura4-D18*	Phong Tran, USA
pREP41-Dnm1-Cterm-GFP (plasmid)	*Dnm1-GFP*	Isabelle Jourdain, UK
pREP41-Dnm1 (plasmid)	*Dnm1 (untagged)*	Isabelle Jourdain, UK

765

766 **Table S2**

767

768 **Partitioning of mitochondria between daughter cells.**

n	*x*	*(n-x)*	*N*	*Obs.*	*Exp.*	*Obs.-Exp.*
5	2	3	2	2	1.25	0.75
6	2	4	2	2	0.94	1.06
	3	3		0	0.63	-0.63
7	4	3	3	3	1.64	1.36
8	2	6	7	1	1.53	-0.53
	3	5		4	3.06	0.94
	4	4		2	1.91	0.09
9	3	6	11	4	3.61	0.39
	4	5		7	5.41	1.59
10	3	7	6	1	1.41	-0.41
	4	6		2	2.46	-0.46
	5	5		3	1.48	1.52
11	4	7	4	1	1.29	-0.29
	5	6		3	1.80	1.20
12	5	7	8	6	3.09	2.91
	6	6		2	1.80	0.20
13	5	8	5	3	1.57	1.43
	6	7		2	2.09	-0.09
14	5	9	7	1	1.71	-0.71
	6	8		4	2.57	1.43
	7	7		2	1.47	0.53
15	6	9	5	2	1.53	0.47
	7	8		3	1.96	1.04
16	6	10	2	1	0.49	0.51
	7	9		1	0.70	0.30
	8	8		0	0.40	-0.40
17	6	11	2	1	0.38	0.62
	7	10		0	0.60	-0.60
	8	9		1	0.74	0.26
18	8	10	1	1	0.33	0.67
	9	9		0	0.37	-0.37

769 *n* is the number of mitochondria in the mother, *x* and *n-x* in the daughter cells at cell
770 division. *N* is the number of cells counted with *n* mitochondria in the mother. *Obs.* is the
771 observed number of cells showing partition of *n* into *x* and *n-x*, and *Exp.* is the expected
772 number of cells with the same *x* and *n-x* partition given *N* cells predicted by the binomial
773 distribution.

Supplementary video captions

Video S1. Live-cell confocal microscopy of MBC-treated interphase fission yeast cells with the mitochondria stained with Mitotracker. Warmer colours indicate higher intensities. Images were acquired at 2min intervals. Time 00:00 (mm:ss) indicates time of addition of MBC. Imaging was resumed 15min after MBC addition ('15:00'). Scale bar represents 2μm. This movie corresponds to Extended Data Fig. 1c.

Video S2. 3D projection of microtubules (green) and mitochondria (magenta) in a wild-type cell (strain KI001, see Table S1). This movie corresponds to Fig. 1a.

Video S3. 3D projection of microtubules (green) and mitochondria (magenta, stained with Mitotracker) in a Klp5Δ/Klp6Δ cell (strain G3B, see Table S1). This movie corresponds to Fig. 1a.

Video S4. 3D projection of microtubules (green) and mitochondria (magenta, stained with Mitotracker) in a Klp4Δ cell (strain G5B, see Table S1). This movie corresponds to Fig. 1a.

Video S5. Mitochondrial dynamics in a wild-type cell (strain KI001, see Table S1) stained with Mitotracker. A 5-slice Z-stack with step size of 0.5μm was obtained every 12s. The video represents the maximum-intensity projected images of the stacks obtained. Warmer colours indicate higher intensity. The closed white arrowhead points to a fusion event and the open white arrowhead points to a fission event. Scale bar represents 2μm. This movie corresponds to Fig. 2a.

Video S6. Mitochondrial dynamics in a Klp5Δ/Klp6Δ cell (strain G3B, see Table S1) stained with Mitotracker. A 5-slice Z-stack with step size of 0.5μm was obtained every 12s. The video represents the maximum-intensity projected images of the stacks obtained. Warmer colours indicate higher intensity. The closed white arrowhead points to a fusion event. Scale bar represents 2μm. This movie corresponds to Fig. 2a.

Video S7. Mitochondrial dynamics in a Klp4Δ cell (strain G5B, see Table S1) stained with Mitotracker. A 5-slice Z-stack with step size of 0.5μm was obtained every 12s. The video represents the maximum-intensity projected images of the stacks obtained. Warmer colours indicate higher intensity. The open white arrowhead points to a fission event. Scale bar represents 2μm. This movie corresponds to Fig. 2a.

Video S8. 3D projection of microtubules (green) and mitochondria (magenta) in a wild-type mitotic cell (strain KI001, see Table S1). This movie corresponds to Fig. 3a.

Video S9. Microtubule dynamics (left) and mitochondrial dynamics (right) in a wild-type cell (KI001, see Table S1) at the onset of mitosis. A 5-slice Z-stack with step size of 0.5μm was obtained every 2min. The video represents the maximum-intensity projected images of the stacks obtained. Warmer colours indicate higher intensity. Scale bar represents 2μm. The open white arrowheads point to fission events. This movie corresponds to Fig. 3b.

820 **Video S10.** 3D projection of Dnm1 (green) and microtubules (magenta) in wild-type cells
821 (strain MTY271 transformed with pREP41-Dnm1-Cterm-GFP, see Table S1). This movie
822 corresponds to Fig. 5a.